

Article

Uncertainty of the X-ray Diffraction (XRD) $\sin^2 \psi$ Technique in Measuring Residual Stresses of Physical Vapor Deposition (PVD) Hard Coatings

Quanshun Luo ^{1,*} and Shicai Yang ²

¹ Materials and Engineering Research Institute, Sheffield Hallam University, Howard Street, Sheffield S1 1WB, UK

² Miba Coating Group, Teer Coatings Ltd., West Stone House, West Stone, Berry Hill Industrial Estate, Droitwich, Worcestershire WR9 9AS, UK; shicai.yang@miba.com

* Correspondence: q.luo@shu.ac.uk; Tel.: +44-114-2253649

Received: 3 July 2017; Accepted: 17 August 2017; Published: 20 August 2017

Abstract: Residual stresses of physical vapor deposition (PVD) hard coatings can be measured using X-ray diffraction (XRD) methods under either conventional $d\text{-}\sin^2 \psi$ mode or glancing incident (GIXRD) mode, in which substantial uncertainties exist depending on the applied diffraction parameters. This paper reports systematic research on the effect of the two analytical modes, as well as the anisotropic elastic modulus, on the measured residual stress values. A magnetron sputtered TiN grown on hardened tool steel was employed as the sample coating, to measure its residual stress using various diffraction peaks from {111} to {422} acquired at a range of incident glancing angles from 2° to 35° . The results were interpreted in terms of the effective X-ray penetration depth, which has been found to be determined predominantly by the incident glancing angle. In the $d\text{-}\sin^2 \psi$ mode, the results present an approximate residual stress over a depth of effective X-ray penetration, and it is recommended to use a diffraction peak of high-index lattice plane from {311} to {422}. The GIXRD mode helps determine a depth profile of residual stress, since the measured residual stress depends strongly on the X-ray penetration. In addition, the anisotropy of elastic modulus shows limited influence on the calculated residual stress value.

Keywords: PVD hard coatings; residual stresses measurement; X-ray diffraction

1. Introduction

Most hard coatings grown by plasma enhanced physical vapor deposition (PVD) show various levels of residual stresses which strongly influence the adhesion and tribological performance. Accordingly, accurate stress measurement is highly desirable. Similar requirements also exist in many other engineering materials, such as surface-hardened turbine blades, gears and spring components.

X-ray diffraction (XRD) is a widely used method of residual stress measurement, namely, by means of the XRD $\sin^2 \psi$ technique [1–4]. A schematic sketch of the method is shown in Figure 1. A crystalline plane is employed as the strain gauge to measure its d -spacing at a series of off-axis angles, ψ , i.e., the angle between the normal of the strain gauge plane to the normal of the sample surface. Then by plotting the d -spacing linearly against the corresponding $\sin^2 \psi$ values, a linear regression is made whereas the slope is used to calculate the lattice strain. In the conventional $\sin^2 \psi$ measurement, a crystal plane, usually having a high diffraction angle ($2\theta > 125^\circ$), is selected as the strain gauge that a series of ψ angles can be obtained by acquiring its diffraction peaks at different incident angles, Ω , of the X-ray beam [4,5]. For thin films or coatings, however, the measurement at such a large diffraction angle always comes with an extremely weak diffraction peak and strong peak broadening. Consequently, crystalline planes of low diffraction angles have also been used.

An alternative method is glancing incident XRD (GIXRD), in which a constant Ω angle of incident X-ray is employed to acquire diffraction peaks of different diffraction angles and thereafter different ψ angles, given the relation between the three angles as $\psi = \theta - \Omega$ [6–12]. The GIXRD method is especially useful in measuring the residual stresses of extremely thin films and surface layers when a very low Ω angle is employed. The GIXRD method has been useful in measuring the residual stresses of thin films and coatings having cubic crystalline structures [9,11,13–16].

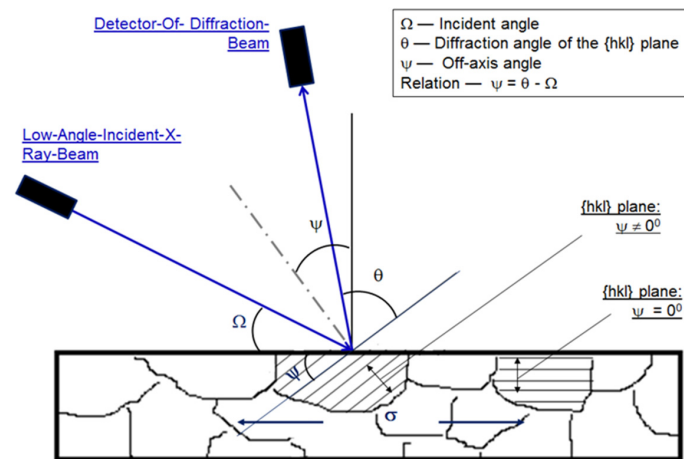


Figure 1. A schematic diagram showing the geometric set-up of X-ray diffraction (XRD) residual stress measurements.

Large uncertainties may arise in residual stress measurements when the applied XRD $\sin^2 \psi$ method results in either a nonlinear d - $\sin^2 \psi$ plot or large scattering in a linear d - $\sin^2 \psi$ plot. In the conventional $\sin^2 \psi$ measurement, for example, Perry and co-workers reported splitting $\sin^2 \psi$ plots in measuring the residual stresses of sputtered titanium nitride coatings by using the {220}, {111} and {200} planes [8]. Kim reported different slopes of the $\sin^2 \psi$ plots between the measurements using {111} and {200} crystal planes of titanium nitride coatings [7]. For the former, the uncertainties may result from both the dependence of X-ray penetration on the applied diffraction geometry, i.e., the Ω and ψ angles and the structural heterogeneity of the films and coatings to be measured. In fact, different crystalline planes, from the low-index planes {111} and {200}, to the high-index planes {311} to {422}, have been employed by many researchers in measuring the residual stresses of TiN coatings [8–11]. Similarly, in the GIXRD method, the incident angle has been also known to have remarkable influence on values of the measured residual stresses because of the variation of X-ray penetration depth [10,12]. Unfortunately, there is a lack of systematic experimental research to clarify and interpret the effect of these geometric factors on stress measurements, although being discussed in theoretical principal [13]. For the latter, because the nano-scale structure heterogeneity of PVD coatings has been experimentally approved as a result of microstructure evolution during their growth, a stress profile is expected to exist along the depth of such a coating. Related to this, theoretical and experimental approaches have been published for the measurement of stress profiles [17–19].

In addition, the anisotropic nature of most crystalline materials also leads to considerable scatter of the calculated stress values because the Young's modulus depends on the crystallographic orientation. In case of transition metal nitrides, a number of papers reported the anisotropic elastic modulus of titanium nitride coatings [8,20–24]. For the data scattering in a linear d - $\sin^2 \psi$ plot, it has been reported that the method of diffraction peak positioning has significant influence on the precision of the linear d - $\sin^2 \psi$ regression and the parabolic method was recommended to give the lowest scattering [25].

In this paper, an assumption of orientation-independent biaxial stress state has been followed to allow the study to be focused on the uncertainties of residual stress measurements arising from the selection of XRD parameters. For this purpose, a magnetron sputtered titanium nitride coating

has been selected as a sample coating to investigate the effect of XRD geometry on the results of residual stress measurement. A series of Ω angles have been employed to acquire diffraction peaks of crystal planes of the nitride ranging from {111} to {422}. In particular, the diffraction angles of most of the employed crystal planes are lower than 125° , the minimum angle for high-accuracy stress measurements recommended in the literature [4,5]. To interpret the obtained results, the relationship between the X-ray penetration depth and the intensity of the diffracted X-ray beam has been calculated as a function of the applied geometrical conditions. It is expected that the results presented could help improve understanding about the accuracy in XRD residual stress measurements, especially the selection of appropriate diffraction parameters.

2. Experimental Procedure and Stress Calculation

2.1. The Sample Material

A stoichiometric titanium nitride coating was grown on a polished coupon surface of pre-hardened (HRC 64) M42 tool steel, by using a four-magnetron close-field unbalanced magnetron sputtering system (self-made equipment, Teer Coatings Ltd., Droitwich, UK). In the reactive sputtering deposition, all the four pure titanium targets were powdered under direct-current magnetron mode where the deposition chamber was maintained with partial pressure of gaseous nitrogen. The deposition procedures started with argon-ion etching on the samples using a pulsed DC power of frequency 350.0 kHz, pulse width 0.5 μ s and a high negative substrate potential of -400 V. Then a thin metallic titanium interlayer, approximately 230 nm thick, was grown at a substrate bias -70 V and the four magnetrons being powered at 3.0 kW. After that, reactive nitrogen gas was introduced to deposit the stoichiometric TiN for 40 min.

Details of the structural characterization and mechanical properties of the sample coating can be found elsewhere [26]. In brief, the coating was 2.56 μ m thick, exhibiting a single-phase cubic crystalline structure with a strong {220} texture and hardness of $HK_{0.025} 34.8 \pm 3.8$ GPa. Figure 2a,b shows the surface morphology of the coating and its microstructure, respectively. In Figure 2a, the coating exhibits a rough surface in sub-micron scale, whereas in Figure 2b the cross-sectional TEM (transmission electron microscopy, CM 20 STEM, Philips, Eindhoven, The Netherlands) micrograph shows dense columnar TiN grains. Note that the Ti interface is shown at the bottom of the cross-sectional micrograph, as labelled in Figure 2b.

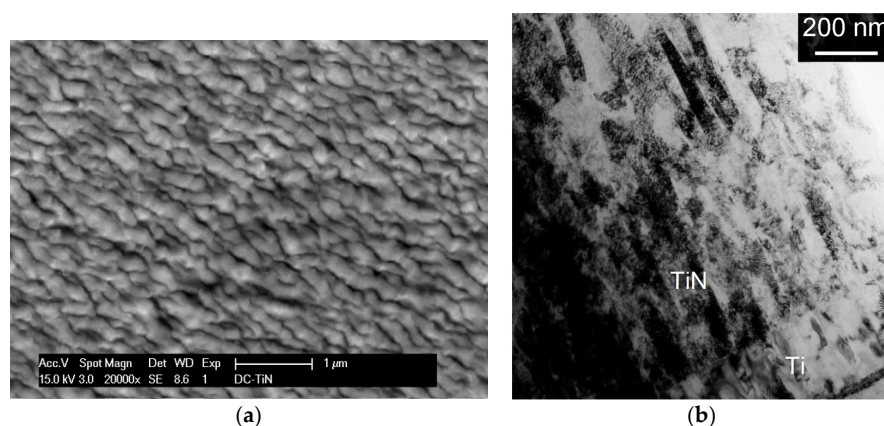


Figure 2. (a) A FEG-SEM (field-emission-gun scanning electron microscopy) micrograph of the TiN coating surface; (b) A cross-sectional TEM bright field micrograph of the TiN coating.

2.2. XRD Experiments

A computer programmed Philips X'Pert X-ray diffraction instrument (Almelo, The Netherlands) was employed, using an incident radiation of $\text{Cu-K}\alpha_1$ ($\lambda = 0.154056$ nm, the copper anode at 40 kV and

40 mA). Figure 1 shows the XRD setup of residual stress measurements. The instrument was run with a PW3050/60 goniometer which could perform both under the $\theta/2\theta$ mode and the glancing angle (GA, or Ω - 2θ) mode with minimum step size of 0.001° . In this work, the incident X-ray was in line-focus and aligned to pass a divergence slit and an anti-scattering slit, both of 0.25° , and a mask window of 10 mm in width. No monochromator was applied so that a fraction of $\text{Cu-K}_{\alpha 2}$ ($\lambda = 0.1544426$ nm) was also included in the incident beam in addition to the $\text{Cu-K}_{\alpha 1}$. In particular, before each XRD scan, the height position of the sample to be analyzed was carefully adjusted using a manufacturer-supplied dial gauge which has a height resolution of 0.002 mm. Diffraction curves were acquired at the Ω - 2θ mode. In this mode, while the incident X-ray hits the sample surface at a fixed angle, Ω , the detector scans over a range to detect diffraction peaks. For each diffraction peak, its off-axis angle ψ is determined by the angle Ω and the diffraction half-angle, θ . In addition, a restriction is applied, that the maximum Ω angle is defined by $\Omega_{\max} = \theta$, since the maximum scanning angle between the beam emission and detection is 180° . Therefore, while a series of fixed Ω angles from 2° to 35° were applied to collect the TiN diffraction peaks from {111} to {422}, the low-index lattice planes {111}, {200} and {220}, and {311} were scanned under the maximum Ω angles of 14° , 18° and 28° , respectively. At each scan, the detector was programmed to scan at a step size of 0.05° and, depending on the Ω angle, acquisition time from 300 to 1500 s to ensure sufficient diffraction beam intensity.

The as-acquired diffraction curves were processed by $\text{K}_{\alpha 2}$ stripping, background removing, 11-point smoothening, and the Lorentz-Polarization-Absorption treatments. A parabolic approach technique of $0.6 I_{\max}$ (I_{\max} denoting the maximum intensity of a diffraction peak) was adopted to determine the diffraction angle, 2θ , as our previous research revealed that parabolic approach ensures the highest precision in peak positioning measurement [25]. Then, using each measured 2θ value, the precise values of the off-axis angle, ψ , crystal plane d-spacing, d , and lattice parameter, a , were deduced accordingly.

2.3. Calculation of Residual Stresses

The equations for residual stress calculation have been well documented in literature, e.g., in [1–6]. An orientation-independent bi-axial stress state is assumed in this paper. In the mechanics of residual stress measurement, the d-spacing of the employed lattice plane $\{hkl\}$, $d_{\{hkl\}}$, is expressed as a linear function of $\sin^2 \psi_{\{hkl\}}$ in Equation (1a), or Equation (1b), where E and ν stand for the Young's modulus and Poisson's ratio, respectively. Note that, the residual stress, σ , and the stress-free lattice spacing, d_0 , are also included in Equation (1a).

In this paper, we have processed the data in two modes, namely the conventional d - $\sin^2\psi$ mode, termed as $\{hkl\}$ mode in short, and the GIXRD mode. In the $\{hkl\}$ mode, the diffraction peaks of a selected $\{hkl\}$ lattice plane are acquired at a range of incident Ω angles, to give rise to a group of $d_{\{hkl\}}$ and $\sin^2\psi_{\{hkl\}}$ values which consequently generate a linear regression using Equation (1a). The linear regression then turns out a set of two constants, C and D , which are expressed as functions of σ and d_0 , seeing Equation (1c,d). Consequently, the values of σ and d_0 can be deduced using Equation (2a,b), respectively. Meanwhile, the linear regression also turns out the deviation of the linear regression slope, ΔC , and the deviation of the linear regression constant, ΔD . Using the obtained σ , d_0 , ΔC and ΔD values, the associated deviations, $\Delta\sigma$ and Δd_0 , can be obtained using Equation (2c,d).

$$d_{\{hkl\}} = \frac{1 + \nu}{E} \times \sigma \times d_0 \times \sin^2 \psi_{\{hkl\}} + \frac{-2 \times \nu}{E} \times \sigma \times d_0 + d_0 \quad (1a)$$

$$d_{\{hkl\}} = C \times \sin^2 \psi_{\{hkl\}} + D \quad (1b)$$

$$C = \frac{1 + \nu}{E} \times \sigma \times d_0 \quad (1c)$$

$$D = \frac{-2 \times \nu}{E} \times \sigma \times d_0 + d_0 \quad (1d)$$

$$\sigma = \frac{E \times C}{(1 + \nu) \times D + 2 \times \nu \times C} \quad (2a)$$

$$d_0 = \frac{2 \times \nu \times C}{(1 + \nu)} + D \quad (2b)$$

$$\Delta\sigma = \frac{(E - 2 \times \nu \times \sigma) \times \Delta C}{(1 + \nu) \times d_0} \times \Delta C - \frac{\sigma}{d_0} \times \Delta D \quad (2c)$$

$$\Delta d_0 = \frac{2 \times \nu \times \Delta C}{(1 + \nu)} \times \Delta C + \Delta D \quad (2d)$$

For the GIXRD method, a simple conversion is made for cubic structured polycrystalline, like the transition metal nitride TiN, by replacing the d-spacing $d_{\{hkl\}}$ with the lattice parameter $a_{\{hkl\}}$. Consequently, Equation (1a) to Equation (2d) can be rewritten as Equation (3a) to Equation (4d), respectively.

$$a_{\{hkl\}} = \frac{1 + \nu}{E} \times \sigma \times a_0 \times \sin^2 \psi_{\{hkl\}} + \frac{-2 \times \nu}{E} \times \sigma \times a_0 + a_0 \quad (3a)$$

$$a_{\{hkl\}} = C \times \sin^2 \psi_{\{hkl\}} + D \quad (3b)$$

$$C = \frac{1 + \nu}{E} \times \sigma \times a_0 \quad (3c)$$

$$D = \frac{-2 \times \nu}{E} \times \sigma \times a_0 + a_0 \quad (3d)$$

$$\sigma = \frac{E \times C}{(1 + \nu) \times D + 2 \times \nu \times C} \quad (4a)$$

$$a_0 = \frac{2 \times \nu \times C}{(1 + \nu)} + D \quad (4b)$$

$$\Delta = \frac{(E - 2 \times \nu \times \sigma) \times \Delta C}{(1 + \nu) \times a_0} \times \Delta C - \frac{\sigma}{a_0} \times \Delta D \quad (4c)$$

$$\Delta a_0 = \frac{2 \times \nu \times \Delta C}{(1 + \nu)} \times \Delta C + \Delta D \quad (4d)$$

In the above calculations, the elastic modulus, E , and Poisson's ratio, ν , are assumed to be constants, namely $E = 456$ GPa and $\nu = 0.2$ [23]. This assumption is necessary and provides feasibility in calculation when its anisotropic elastic property is unknown. However, the assumption of constant E modulus has been claimed to contribute to the non-linear d - $\sin^2 \psi$ plots or linear plots with different slopes [7,8,27]. To tackle this problem, a new treatment was introduced in literature [14], in which the anisotropic $E_{\{hkl\}}$ varies depending on the different crystal planes $\{hkl\}$ in a phase

$$f_{\{hkl\}} = \left(\frac{(1 + \nu)}{E_{\{hkl\}}} \times \sin^2 \psi_{\{hkl\}} - \frac{2\nu}{E_{\{hkl\}}} \right)$$

The modified equation of Equation (3a) is written in Equation (5). The anisotropic elastic properties of transition metal nitrides were reported in literature [7,22–24,27]. In this paper, we have adopted the orientation-dependent E values of TiN determined by ab initio calculation, shown in Table 1 [22].

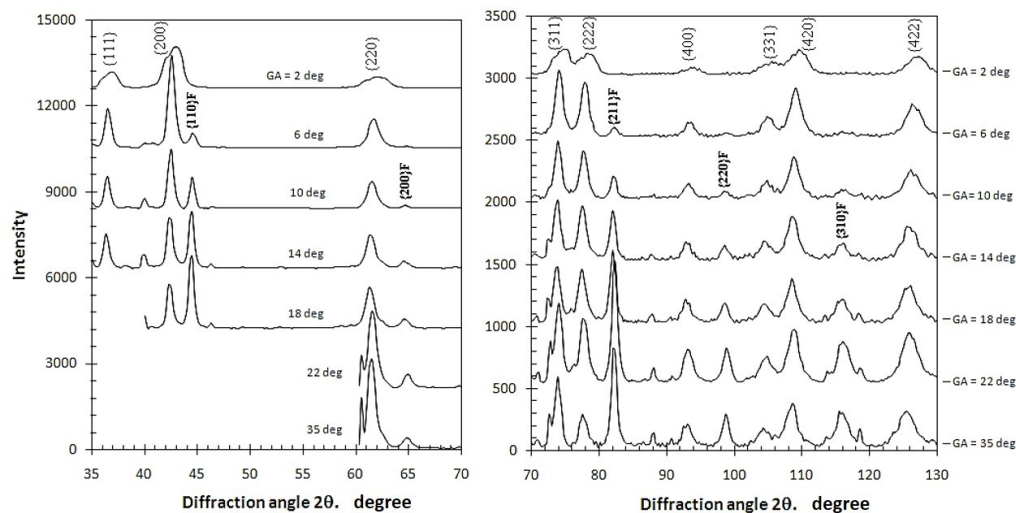
$$a_{\{hkl\}} = \left(\frac{(1 + \nu)}{E_{\{hkl\}}} \times \sin^2 \psi_{\{hkl\}} - \frac{2 \times \nu}{E_{\{hkl\}}} \right) \times \sigma \times a_0 + a_0 \quad (5)$$

Table 1. The Young's modulus values of TiN [22].

Lattice Plane	E [GPa]
{111}, {222}	417
{200}, {400}	451
{111}, {222}	424
{200}, {400}	434

3. Results and Discussion

Figure 3 shows a collection of the obtained diffraction curves at various Ω angles of 2° – 35° , showing the diffraction peaks of TiN from {111}, {200}, to {422}. Moreover, it has been noticed that, except for the curve acquired at a very low Ω angle of 2° , several diffraction peaks of the substrate ferrite are also visible, which provides evidence that the incident and diffracted X-rays transmitted across the whole TiN section. In other words, the whole TiN coating section contributed to each diffraction peak. Table 2 lists all the measured values of the diffraction peaks, which are consequently employed to analyze the residual stress characteristics in the following sections.

**Figure 3.** Diffraction curves acquired at various Ω angles (GA refers to glancing angle Ω).**Table 2.** The measured peak positions, 2θ , of the TiN crystalline planes from {111} to {422} at various incident Ω angles (degree).

Ω	{111}	{200}	Ω	{220}	{311}	{222}	{400}	{331}	{420}	{422}
2	36.93	42.96	2	62.16	74.74	78.35	93.85	105.75	109.55	127.00
4	36.62	42.67	6	61.71	74.07	77.87	93.39	105.01	109.07	126.54
6	36.56	42.61	10	61.55	73.92	77.69	93.20	104.80	108.82	126.23
8	36.51	42.55	14	61.49	73.85	77.57	93.08	104.71	108.69	126.04
10	36.49	42.53	18	61.41	73.80	77.50	92.99	104.56	108.56	125.81
12	36.49	42.50	22	61.42	73.82	77.51	92.98	104.51	108.60	125.75
14	36.46	42.50	28	61.31	73.69	77.40	92.75	104.21	108.37	125.26
16	36.46	42.49	35	–	–	77.42	92.77	103.96	108.11	124.88
18	–	42.48	–	–	–	–	–	–	–	–

3.1. Residual Stresses Measured under the {hkl} Mode

Figure 4 shows the $a_{\{hkl\}}$ versus $\sin^2 \psi$ plots for various TiN planes from {111} to {422}. The use of $a_{\{hkl\}}$ instead of $d_{\{hkl\}}$ allows straightforward comparison between the results obtained from various {hkl} planes. Note that the vertical axis is defined with a constant scale, seeing the scale bar of the axis, but without exact value, so that the as-measured $a_{\{hkl\}}$ values in each group can be plotted versus the $\sin^2 \psi$

values to show their match to a linear regression. It can be found that good linear relationships exhibit in all the data groups, except that the $a_{\{hkl\}}$ values obtained at the lowest incident beam angle $\Omega = 2^\circ$ (the last data point in each series) are extraordinarily lower and off-line as compared to other data. The extraordinary values were attributed to the substantially low X-ray penetration at the extremely low Ω angle, to be discussed in a later section. Thus, the last data points were excluded when all the other points were processed to set up a group of linear regressions according to Equation (1a). After that, the two constants deduced from each linear regression were employed in Equation (1b,c) to calculate the residual stress, σ , and the stress-free lattice parameter, a_0 . The results are listed in Table 3. All the regressions obey good linear relationships with a high linear precision coefficient $R^2 > 0.9$. The obtained values of the residual stress and the stress-free lattice parameter are plotted in Figure 5.

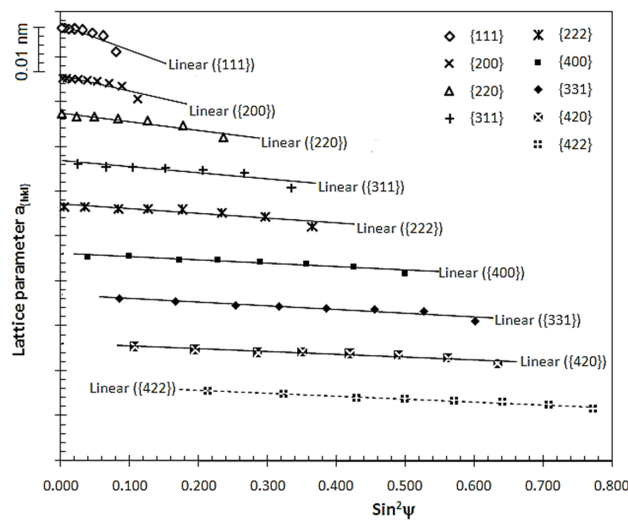


Figure 4. The $a_{\{hkl\}}$ vs. $\sin^2 \psi$ plots for various lattice planes of TiN calculated under the $\{hkl\}$ mode.

Table 3. Results of calculations at the $\{hkl\}$ mode.

Parameters	{111}	{200}	{220}	{311}	{222}	{400}	{331}	{420}	{422}
Slope (10^{-2})	-3.06	-2.05	-1.28	-0.68	-0.70	-0.57	-0.65	-0.50	-0.61
R^2	0.96	0.95	0.96	0.91	0.92	0.95	0.97	0.95	0.99
σ (MPa)	-17,999	-11,974	-7383	-3917	-4002	-3276	-3713	-2865	-3504
$\Delta\sigma$ (MPa)	1667	1083	809	611	535	340	276	292	184
a_0 (nm)	0.4152	0.4178	0.4224	0.4236	0.4243	0.4239	0.4241	0.424	0.4246

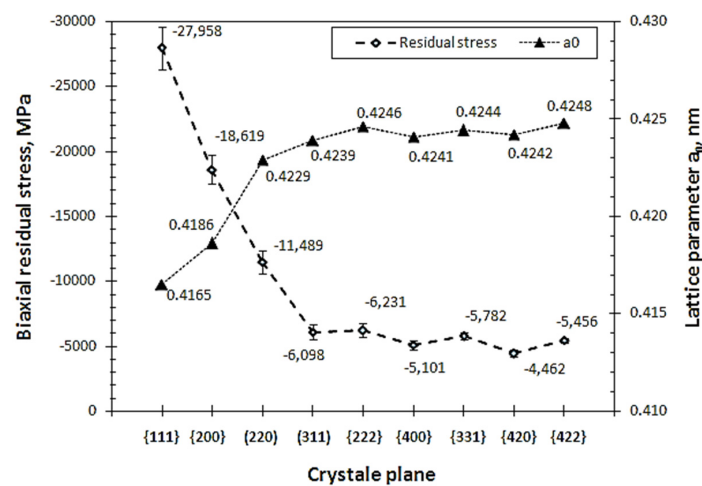


Figure 5. Residual stresses and stress-free lattice parameters of the TiN following the $\{hkl\}$ mode.

In Figure 5, the high-angle diffraction peaks from {311} to {422} give similar values of residual stress in a range of $-4.46\sim-6.23$ GPa, each with a small deviation, $\Delta\sigma$. In particular, the calculated residual stress is irrelevant to the employed lattice planes. Meanwhile, the calculated stress-free lattice parameter, a_0 , is stabilized in a small range of $0.4239\sim0.4248$ nm, being comparable to the values reported in the literature [8,9,14,20]. On the other hand, the calculations from the three low-index planes {220}, {200} and {111} produce extraordinarily high residual stresses, namely -11.5 , -18.6 and -28.0 GPa, respectively. Accordingly, the calculated lattice parameters vary from 0.4229 nm to 0.4165 nm, which are systematically smaller than those calculated at high-index planes.

Using the measured orientation-dependent lattice parameters $a_{\{hkl\}}$ (Figure 4) and the calculated stress-free lattice parameters a_0 (Figure 5), the orientation-dependent residual strains $\varepsilon_{\{hkl\}}$, $\varepsilon_{\{hkl\}} = (a_{\{hkl\}} - a_0)/a_0$, have been estimated as a function of the employed crystal plane $\{hkl\}$, the incident Ω angle, and the ψ angle. The results are displayed in Figure 6. For the measurements of high-index $\{hkl\}$ planes, the strains exhibit a similar linear relationship with respect to the $\sin^2 \psi$, with their values falling in a range of $\varepsilon = +0.05\sim-0.06$. However, the three low-index planes {111}, {200} and {220} show much higher strain values. These values depend strongly on the $\{hkl\}$ plane. In addition, it is also noticed that substantially different results were obtained from the {111} and {222} diffractions although they refer to the same groups of crystal planes; similarly large differences also exist between the results from the {200} and {400} diffractions. These differences are to be discussed in the next section. Nevertheless, the results suggest that only high-angle diffraction peaks are suitable for residual stress measurement although it is not technically necessary to select a diffraction peak of $2\theta > 125^\circ$ [4].

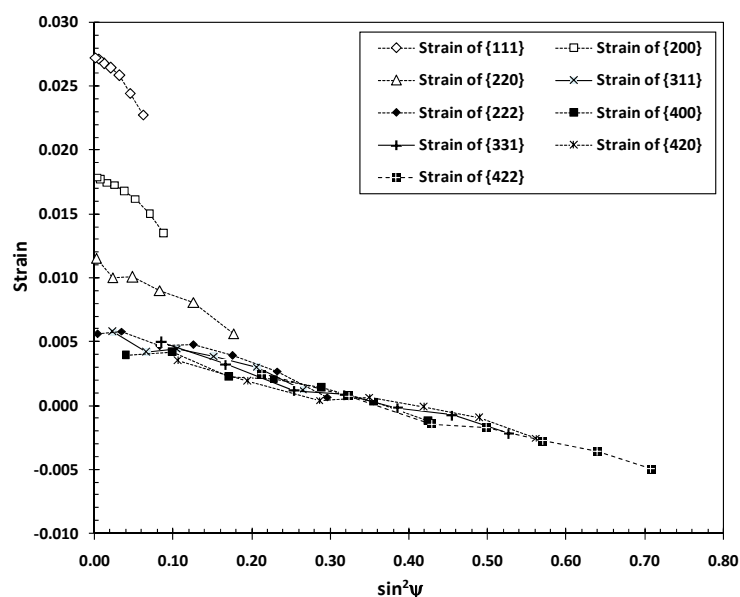


Figure 6. Residual strains estimated as a function of both the employed lattice plane $\{hkl\}$ and the off-axis angle ψ .

3.2. Residual Stresses Measured under the GIXRD Mode

Following the GIXRD method, the measured lattice parameter $a_{\{hkl\}}$ were plotted against the $\sin^2 \psi$ for the applied Ω angles from 2° to 35° . Results of the linear regressions are shown in Table 4. Figure 7 shows the plots. Similar to the chart in Figure 4, the vertical axis is drawn with a constant scale instead of exact value, so that the as-measured $a_{\{hkl\}}$ values in each group can be plotted versus the $\sin^2 \psi$ values to show their match to a linear regression. Most of the plots, for $\Omega = 2^\circ\sim 28^\circ$, show fairly good linear relationships although the precision factors, R^2 , in a range of $0.69\sim 0.82$, are considerably lower than those obtained using the $\{hkl\}$ mode as shown in Table 3. However, the slopes show substantially different values depending on the Ω angle. Whereas most slopes are negative giving rise

to compressive stresses, the data acquired at the smallest Ω angle of 2° leads to a positive slope and a tensile residual stress. The different values of the calculated slope, ranging between -6.82×10^{-3} and 0.64×10^{-3} , indicate larger data scattering when the GIXRD mode is applied. The values of residual stress and stress-free lattice parameter are shown in Figure 8.

Table 4. Results of calculations at the glancing incident (GIXRD) mode.

Incident Angle	2	6	10	14	18	22	28	35
Slope (10^{-3})	0.64	-3.70	-4.46	-4.91	-4.78	-6.34	-6.82	-3.46
R^2	0.08	0.82	0.81	0.8	0.69	0.82	0.74	0.29
σ (MPa)	579	-3313	-3994	-4394	-4280	-5677	-6103	-3097
$\Delta\sigma$ (MPa)	759	588	723	845	1172	1215	1633	2783
a_0 (nm)	0.4215	0.4239	0.4244	0.4245	0.4246	0.4242	0.4244	0.4251

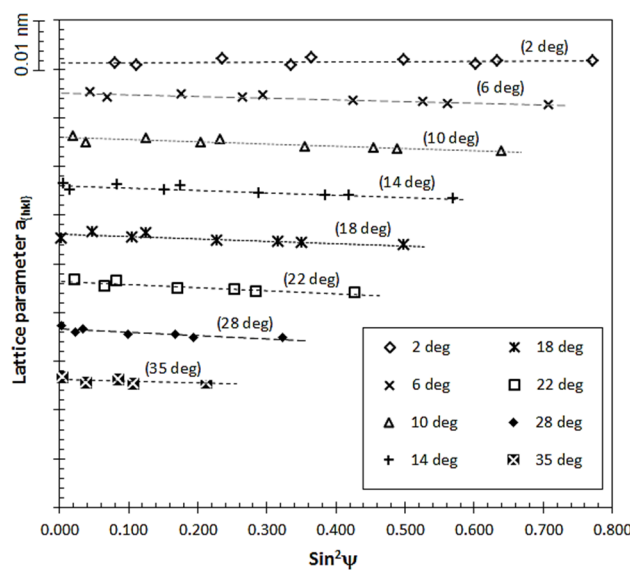


Figure 7. The $a_{\{hkl\}}$ vs. $\sin^2 \psi$ plots for various Ω angles calculated under the GIXRD mode.

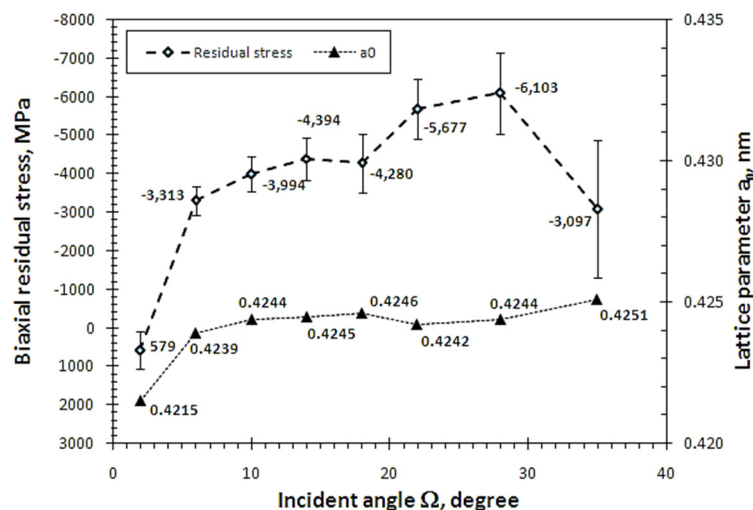


Figure 8. Effect of incident angle Ω on the residual stress and stress-free lattice parameter measured following the GIXRD mode.

The applied Ω angle shows pronounced influence on both the measured residual stress and the stress-free lattice parameter. In the middle Ω range, the measured residual stresses are compressive

and exhibit a linear increase with increasing Ω angle, namely, from -3.13 to -6.10 GPa. Meanwhile, the calculated stress-free lattice parameter a_0 shows values in a narrow range of 0.4239 – 0.4246 nm, which are consistent to the measurements under the $\{hkl\}$ mode (Table 3 and Figure 5) and do not vary with the Ω angle. The consistent a_0 values reveal good chemical homogeneity of the nitrogen concentration across the whole coating section, since the lattice parameter of TiN is known to be determined predominantly by its Ti:N ratio.

At the smallest incident angle of 2° , however, the $a_{\{hkl\}}$ vs. $\sin^2\psi$ plot turns out a poor linear relation with very low regression precision of $R^2 = 0.08$, seeing Figure 7 and Table 4. Surprisingly, it derives a tensile residual stress of 579 MPa, along with a lattice parameter of 0.4215 nm, substantially lower than other measurements. The plot obtained at the highest incident angle 35° is also poorly linear with a low R^2 value of 0.29 . The measured residual stress is -3.10 GPa, lower than those measured at lower incident angles.

3.3. Effect of X-ray Attenuation on the Results of Residual Stress Calculation

The results confirm strong influence of the selected XRD geometric parameters on the stress calculations. The relationships could be understood if the factor of X-ray attenuation is considered. In the XRD data acquisition, X-rays penetrate to the surface only in a limited depth because of the mass attenuation as a result of inelastic scattering, heat generation, and excitation of photoelectrons, etc.

The mass attenuation of X-ray in a diffraction process is schematically shown in Figure 9. An incident X-ray array of initial intensity I_0 hits the sample surface at an incident angle Ω . After travelling to a depth t , its intensity is attenuated to I_1 and causes a diffraction array from the lattice plane $\{hkl\}$ with a diffraction angle 2θ . Then, considering the mass attenuation, the intensity of the diffraction array emitting out of the sample surface, I_z , can be expressed as a function of the total transmission distance, z , the mass density of the sample solid, ρ , and the mass absorption coefficient, μ/ρ , in Equation (6) [2]. According to the simple geometry as shown in Figure 9, the transmission length z is determined by the depth t , and the angles Ω and 2θ . An equation can be drawn, as shown in Equation (7), to calculate the X-ray diffraction intensity I_z generated at the depth t . Then, for a given set of Ω and 2θ angles, the normalized diffraction intensity, I_z/I_0 , can be calculated using to Equation (7) to plot as a function of the depth, t . Selected results are illustrated in Figure 10.

$$I_z = I_0 \times e^{(-1 \times \mu/\rho) \times \rho \times z} \quad (6)$$

$$I_t = I_0 \times e^{-\mu \times (\frac{t}{\sin \Omega} + \frac{t}{\sin(2\theta - \Omega)})} \quad (7)$$

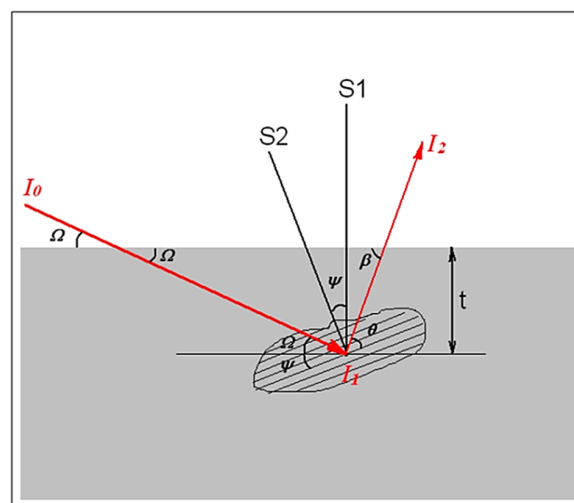


Figure 9. A schematic sketch showing mass attenuation of X-ray in a diffraction process.

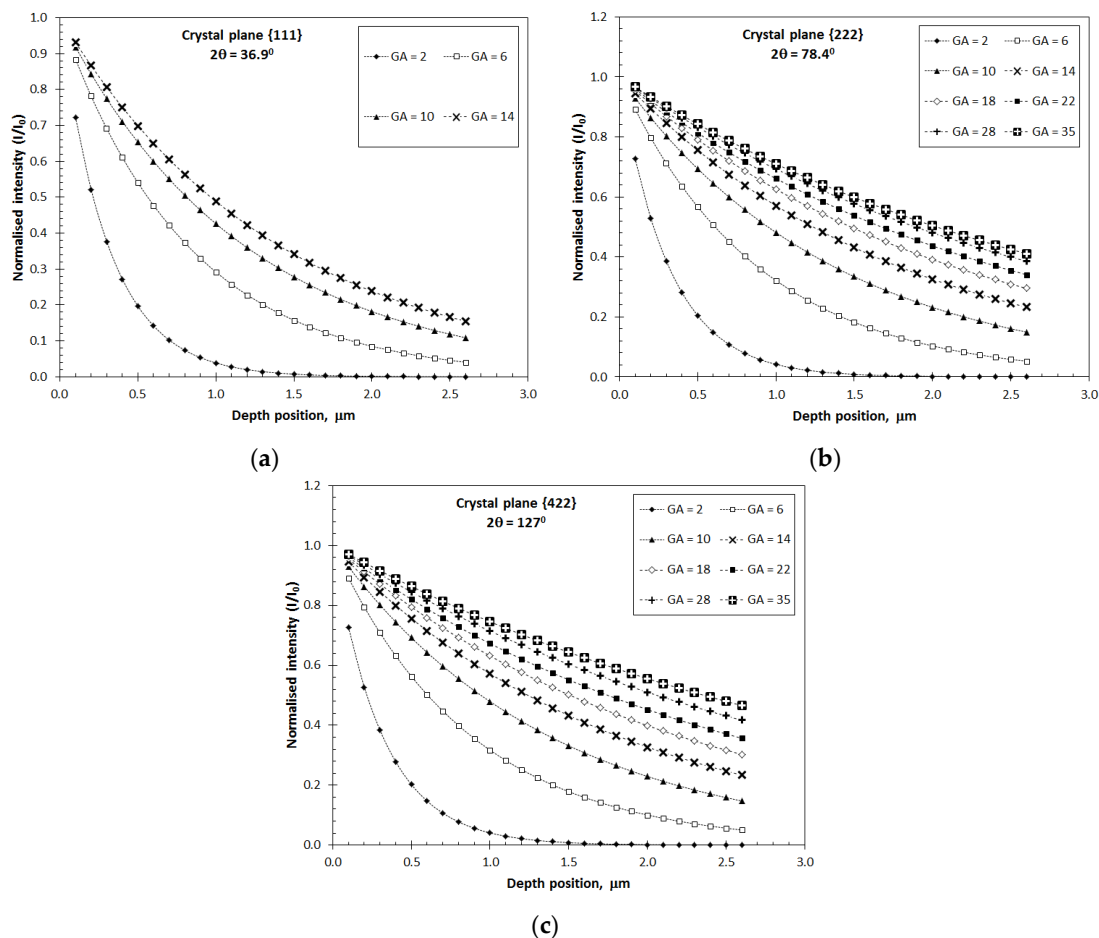


Figure 10. The calculated depth profiles of X-ray penetration (normalised diffraction beam intensity, I/I_0) as functions of both the incident angle Ω (GA, or glancing angle, as shown in the legend) and the diffraction angle 2θ . (a) The depth profiles for various Ω angles for the {111} plane; (b) the depth profiles for various Ω angles for the {222} plane; (c) the depth profiles for various Ω angles for the {422} plane.

In Figure 10, a general trend is that the diffraction intensity attenuates with the increased depth position. The intensity profile for a given set of Ω and 2θ angles represents the different contributions of small volumes at different depths to the sum of the detected diffraction intensity. In other words, the top surface always contributes more than the subsurface region. Moreover, Figure 10 also reveals that the rate of attenuation depends strongly on the applied Ω and 2θ angles, especially the former. At a low Ω angle, the normalized diffracted intensity drops quickly with sample depth, whereas the dropping rate becomes slower when the incident Ω angle becomes higher. Therefore, the relative contribution at a subsurface depth contributes increasingly more with increasing Ω angle. Similarly, the depth profile is also influenced by the diffraction angle, i.e., the employed lattice plane. For the diffractions acquired from a plane of higher index number, e.g., {422} and {222} as shown in Figure 10b,c, most depth profiles show less dependence on the penetration depth. In other words, the detected diffraction is an integration of those generated from the whole coating section although the contribution depends on the depth position.

Such variation of the X-ray penetration depth can be illustrated more quantitatively as a function of the Ω and 2θ angles. If the X-ray penetration depth is defined as the depth to generate a normalized intensity of $I_z/I_0 = 0.36$, it is possible to estimate the depth as a function of the applied Ω and 2θ angles. The results are displayed in Figure 11.

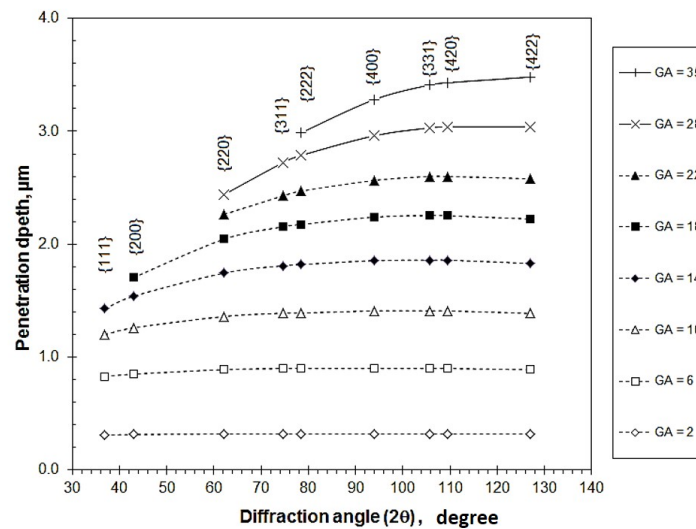


Figure 11. Effective penetration depths as a function of the applied incident Ω angle and the selected diffraction 2θ angle.

Bearing in mind that the intensity of each acquired diffraction peak is actually an integration of the crystalline diffractions generated at a range of depth, Figure 11 would be helpful in interpreting the residual stresses measured under the two modes, i.e., the $\{hkl\}$ mode and the GIXRD mode.

In the $\{hkl\}$ mode, the effective penetration depth for each employed lattice plane varies in a range depending on the applied Ω angle. The Ω -dependent penetration implies that the diffraction peaks acquired in each group were generated from different volumes. Given the depth-dependent heterogeneity of the coating structure, it should be understood that the measured residual stress is an approximate estimation of the overall residual stress instead of an accurate measurement. Nevertheless, such estimated residual stress is acceptable only when a high-angle diffraction peak is employed to allow sufficient X-ray penetration depth. For the high-index planes from $\{222\}$ to $\{422\}$ where the diffraction angle (2θ) is higher than 70° , the X-ray penetration depths are comparable to each other and relatively independent to the employed $\{hkl\}$ plane, whereas most the diffractions were generated from the whole coating section. This may give a reasonable explanation of the comparable residual values obtained from high-angle $\{hkl\}$ diffractions, Figure 5.

The results in Figure 5 suggest that it is not recommended to use low index planes in residual stress measurements. Although it is not in the scope of this paper to give an extensive explanation to the extraordinary values calculated from the $\{111\}$, $\{200\}$ and $\{220\}$ planes, perhaps an important factor can be the lower a_0 values, because the residual stress values were calculated using Equation (2a), in which the residual stress σ increases with the decrease of the constant D and, in Equation (1d), D varies linearly with d_0 .

In addition, considering the strong dependence of penetration depth on the Ω angle, it is recommended to avoid using a low Ω angle. In the previous section, it has been mentioned that the data acquired at the lowest Ω angle were precluded in the stress calculation, because obviously these diffractions were emitted from a very thin surface layer and therefore cannot represent the straining behavior of the whole coating thickness range.

Thus, it is possible to explain the different residual stress values measured from the $\{111\}$ and $\{222\}$ planes and from the $\{200\}$ and $\{400\}$ planes. The penetration depths of the $\{111\}$ and $\{222\}$ diffraction peaks are in the ranges of $0.31\text{--}1.43\ \mu\text{m}$ and $0.32\text{--}2.99\ \mu\text{m}$, respectively. The low-index diffraction peaks represent the straining behavior of the thin top coating instead of the whole thickness range. More importantly, the penetration depth also depends strongly on the applied Ω angle. Thus, the calculated residual stresses are significantly overestimated because of the heterogeneous growth structure of the sputtered coating.

In the GIXRD mode, as shown in Figure 11, the X-ray penetration depth depends mainly on the Ω angle regardless of the $\{hkl\}$ plane. In other words, the diffraction peaks acquired at each Ω angle were from the same depth, which is consistent with the analytical results of other researchers [13–16]. Therefore, the calculated residual stress value each represents an integrated stress value at certain coating thickness. Considering the fact that most hard coatings exhibit heterogeneous structure depending on the plasma-assisted growth [16–21,26,28,29], the GIXRD mode has provided an opportunity to analyze the depth profile of residual stresses, which also helps improve the understanding of the heterogeneous structure.

At the lowest incident Ω angle of 2° , the measured residual tensile stress and the substantially smaller lattice parameter a_0 are substantially different from those determined at higher Ω angles. Because the intensity decreases quickly with increasing depth, the X-ray penetration was restrained in a small depth of $0.3\ \mu\text{m}$. Therefore, the obtained diffractions should represent merely the crystallographic property of the close vicinity of the coating surface. To the knowledge of the authors, there has been no literature which addressed the unusual residual stresses experimentally measured in the extreme surface layer of sputtered TiN coatings. Instead, the formation of tensile residual stresses in the initial growth of thin films has been reported to be related to the constrained shrinkage when individual islands begin to coalesce to each other [30–32]. It is known that the atomic stacking structure of the as-grown coating surface differs greatly to the inner volume, seeing its roughness in atomic and nano scales in Figure 2. In literature, it has been reported that a T-type sputtered coating exhibits dense columnar grains and sub-dense grain boundaries, in which the atomic interaction forces between two adjacent grains result in localized shrinkage and tensile residual stresses [33]. Such tensile stresses at the grain boundaries are combined with the ion-peening induced compressive stresses inside the dense grains to result in a decreased overall compressive residual stress [21,28]. These may partially explain the different residual stresses as measured at the low incident Ω angle, whereas further detailed explanation is beyond the scope of this paper.

When the Ω angle is higher than 10° , the measured a_0 values become more stabilized, which may imply homogeneous nitrogen concentration of the TiN coating. The increased residual stress with increasing Ω angle shows strong evidence of a stress profile along the depth direction. Because the X-ray penetration depth depends almost only on the applied Ω angle and each diffraction peak acquired at a certain Ω angle is actually the integration of diffractions of small volumes within a depth defined by the Ω angle, it is needed to consider a method of analysis to determine a depth profile of the actual residual stress, such as in literature [17–19]. Obviously, more extensive data processing is required, which is beyond the focus of this paper. In brief, the GIXRD mode provides a valuable analytical method to investigate the residual stress distribution in a heterogeneous coating system. The residual stress can be expressed as a function of the applied Ω angle or X-ray penetration depth, instead of a single value.

3.4. Effect of Anisotropic Elastic Modulus on the Calculated Residual Stress Values

Figure 12 illustrates the effect of the adopted Young's modulus values on the calculated residual stresses both following the conventional $\{hkl\}$ mode and the GIXRD mode. In Figure 12a, the residual stress values are compared between the two adopted constant E values, namely, 456 GPa and 300 GPa. Obviously, the higher E value leads to larger values of the calculated residual stress for its linear relation to the elastic modulus, Equations (1) and (3). Similar relations are also obtained in the residual stress values calculated out of the GIXRD mode, as shown in Figure 12b. For both measurement modes, Figure 12a,b show limited influence of the anisotropic E values on the calculated residual stress values. All the values are slightly lower than those obtained from the constant E value of 456 GPa, but substantially higher than those from the E value of 300 GPa. These are not difficult to understand as the adopted anisotropic E modulus, in the range of 417–451 GPa, are close to the higher constant E value of 456 GPa.

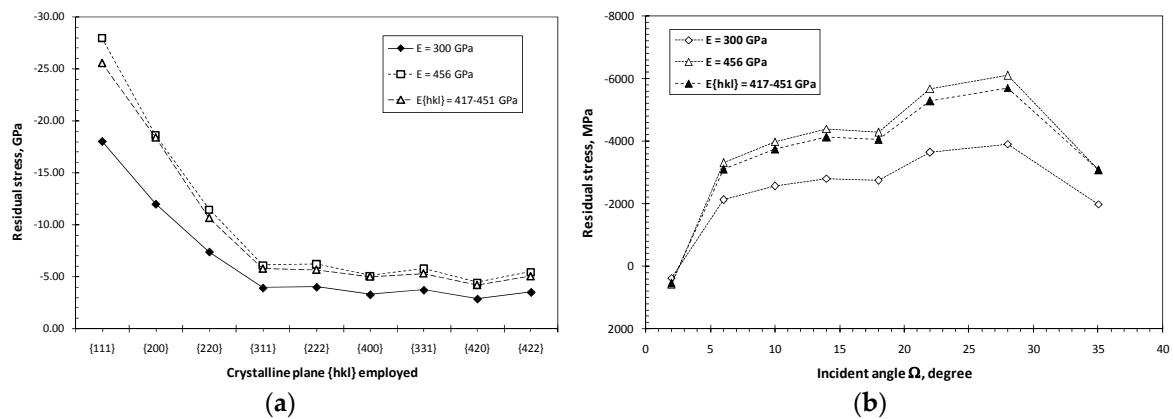


Figure 12. Effect of Young's modulus on the calculated residual stress values. (a) The plots of the calculated stress values versus the employed $\{hkl\}$ planes for the $\{hkl\}$ mode; and (b) the plots of the calculated stress values versus the Ω angles for the GIXRD mode.

The comparison, as shown in Figure 12, suggests that it is generally acceptable to adopt a constant or isotropic E value in the calculation of residual stresses, especially when the aim is to investigate the influence of different deposition processes or between different coating conditions [6,8–10,14–16,28,29]. However, one should be careful if the residual stresses of thin films or coatings are to be compared when they are calculated by using different E values.

4. Conclusions

Using a magnetron sputtered TiN coating, we have experimentally investigated the uncertainty of XRD residual stress measurements as a function of several factors. The results have been interpreted along with the calculation of effective X-ray penetration. The following conclusions can be made.

- The incident Ω angle has decisive influence on the effective X-ray penetration that the penetration increases significantly with the increase of the Ω angle. On the other hand, for a given Ω angle, the effect of the employed diffraction angle 2θ , i.e., the $\{hkl\}$ crystalline plane, is negligible.
- When measuring using the conventional $d\text{-sin}^2\psi$ mode, it is necessary to select a lattice plane of high diffraction angle. The results present the approximate estimation of overall residual stress over the depth of effective X-ray penetration. In the case of TiN coating, as shown in the current study, the residual stresses measured from the diffraction peaks of high-index planes from {311} to {422} are comparable to each other. On the other hand, measurements from the low-index planes {111}, {200} and {220} give rise to extraordinarily high values.
- When measuring using the GIXRD mode, the calculated residual stress depends strongly on the X-ray penetration depth as predominantly determined by the incident Ω angle. This method helps determine a depth profile of residual stress in a coating of heterogeneous growth structure.
- The anisotropy of elastic modulus has a certain influence on the calculation of residual stress, while the influence is not pronounced as compared to the incident Ω angle.

Author Contributions: Quanshun Luo and Shicai Yang designed the experimental research; Shicai Yang deposited the sample TiN coatings; Quanshun Luo carried out the XRD experiments and data analyses; Quanshun Luo and Shicai Yang wrote the paper and carried out the revisions.

Conflicts of Interest: The authors declare no conflict of interest.

References

1. Cullity, B.D.; Stock, S.R. *Elements of X-ray Diffraction*, 3rd ed.; Prentice Hall: Upper Saddle River, NJ, USA, 2001; p. 435.
2. Noyan, I.C.; Cohen, J.B. *Residual Stress—Measurement by Diffraction and Interpretation*; Springer: New York, NY, USA, 1987; pp. 117–163.
3. Malhotra, S.G.; Rek, Z.U.; Yalisove, S.M.; Bilello, J.C. Analysis of thin film stress measurement techniques. *Thin Solid Films* **1997**, *301*, 45–54. [[CrossRef](#)]
4. Fitzpatrick, M.E.; Fry, A.T.; Holdway, P.; Kandil, F.A.; Shackleton, J.; Suominen, L. *Measurement Good Practice Guide No. 52. Determination of Residual Stresses by X-ray Diffraction—Issue 2*; National Physical Laboratory: London, UK, 2006.
5. Portinha, A.; Teixeira, V.; Carneiro, J.; Beghi, M.G.; Bottani, C.E.; Franco, N.; Vassen, R.; Stoeber, D.; Sequeira, A.D.L. Residual stresses and elastic modulus of thermal barrier coatings graded in porosity. *Surf. Coat. Technol.* **2004**, *188–189*, 120–128. [[CrossRef](#)]
6. Scardi, P.; Polonioli, P.; Ferrari, S. Residual stress in stabilized zirconia thin films prepared by RF magnetron sputtering. *Thin Solid Films* **1994**, *253*, 349–355. [[CrossRef](#)]
7. Kim, J.O.; Achenbach, J.D.; Mirkarimi, P.B.; Shinn, M.; Barnett, S.A. Elastic constants of single-crystal transition-metal nitride films measured by line-focus acoustic microscopy. *J. Appl. Phys.* **1992**, *72*, 1805–1811. [[CrossRef](#)]
8. Perry, A.J.; Jagner, M.; Sproul, W.D.; Rudnik, P.J. The residual stress in TiN films deposited onto cemented carbide by high-rate reactive sputtering. *Surf. Coat. Technol.* **1989**, *39–40*, 387–395. [[CrossRef](#)]
9. Quaeysaegens, C.; Knuyt, G.; Stals, L.M. Study of the residual macroscopic stress in TiN coatings deposited on various steel types (TuSA1). *Surf. Coat. Technol.* **1995**, *74–75*, 104–109. [[CrossRef](#)]
10. Liu, H.; Xu, Q.; Zhang, X.; Wang, C.; Tang, B. Residual stress analysis on TiN film fabricated by plasma immersion ion implantation and deposition process. *Nucl. Instrum. Methods Phys. Res.* **2013**, *297*, 1–6. [[CrossRef](#)]
11. Hohl, F.; Stock, H.-R.; Mayr, P. Examination of residual stress, morphology and mechanical properties of sputtered TiN films. *Surf. Coat. Technol.* **1992**, *54–55*, 160–166. [[CrossRef](#)]
12. Saerens, A.; Houtte, P.V.; Meert, B.; Quaeysaegens, C. Assessment of different X-ray stress measuring techniques for thin titanium nitride coatings. *J. Appl. Crystallogr.* **2000**, *33*, 312–322. [[CrossRef](#)]
13. Welzel, U.; Ligot, J.; Lamparter, P.; Vermeulen, A.C.; Mittemeijer, E.J. Stress analysis of polycrystalline thin films and surface regions by X-ray diffraction. *J. Appl. Crystallogr.* **2005**, *38*, 1–29. [[CrossRef](#)]
14. Benegra, M.; Lamas, D.G.; de Rapp, M.E.F.; Mingolo, N.; Kunrath, A.O.; Souza, R.M. Residual stresses in titanium nitride thin films deposited by direct current and pulsed direct current unbalanced magnetron sputtering. *Thin Solid Films* **2006**, *494*, 146–150. [[CrossRef](#)]
15. Skrzypek, S.J.; Baczmanski, A.; Ratuszek, W.; Kusior, E. New approach to stress analysis based on grazing-incident X-ray diffraction. *J. Appl. Crystallogr.* **2001**, *34*, 427–435. [[CrossRef](#)]
16. Lewis, D.B.; Wadsworth, I.; Münz, W.D.; Kuzel, R., Jr.; Valvoda, V. Structure and stress of TiAlN/CrN superlattice coatings as a function of CrN layer thickness. *Surf. Coat. Technol.* **1999**, *116–119*, 284–291. [[CrossRef](#)]
17. Genzel, C. X-ray stress analysis in presence of gradients and texture. *Adv. X-ray Anal.* **2001**, *44*, 247–257.
18. Marques, M.J.; Dias, A.M.; Gergaud, P.; Lebrun, J.L. A methodology development for the study of near surface stress gradients. *Mater. Sci. Eng.* **2000**, *287*, 78–86. [[CrossRef](#)]
19. Jegou, S.; Christiansen, T.L.; Klaus, M.; Genzel, C.; Somers, M.A.J. Determination of composition, residual stress and stacking fault depth profiles in expanded austenite with energy-dispersive diffraction. *Thin Solid Films* **2013**, *530*, 71–76. [[CrossRef](#)]
20. Machunze, R.; Janssen, G.C.A.M. Stress and strain in titanium nitride thin films. *Thin Solid Films* **2009**, *517*, 5888–5893. [[CrossRef](#)]
21. Janssen, G.C.A.M.; Kamminga, J.D. Stress in hard metal films. *Appl. Phys. Lett.* **2004**, *85*, 3086–3088. [[CrossRef](#)]
22. Zhang, M.; He, J. Ab-initio calculation of elastic constants of TiN. *Surf. Coat. Technol.* **2001**, *142–144*, 125–131. [[CrossRef](#)]
23. Sue, J.A. X-ray elastic-constants and residual-stress of textured titanium nitride coating. *Surf. Coat. Technol.* **1992**, *54*, 154–159. [[CrossRef](#)]

24. Abadias, G. Stress and preferred orientation in nitride-based PVD coatings. *Surf. Coat. Technol.* **2008**, *202*, 2223–2235. [[CrossRef](#)]
25. Luo, Q.; Jones, A.H. High-precision determination of residual stress of polycrystalline coatings using optimised XRD- $\sin^2\psi$ technique. *Surf. Coat. Technol.* **2010**, *205*, 1403–1408. [[CrossRef](#)]
26. Luo, Q.; Yang, S.; Cooke, K.E. Hybrid HIPIMS and CFUBMS deposition of TiN coatings: Deposition rate, structure and tribological properties. *Surf. Coat. Technol.* **2013**, *236*, 13–21. [[CrossRef](#)]
27. Leeuwen, M.V.; Kamminga, J.D.; Mittemeijer, E.J. Diffraction stress analysis of thin films: Modeling and experimental evaluation of elastic constants and grain interaction. *J. Appl. Phys.* **1999**, *86*, 1904–1915. [[CrossRef](#)]
28. Luo, Q.; Lewis, D.B.; Hovsepian, P.E.; Münz, W.-D. Transmission electron microscopy and X-ray diffraction investigation of the microstructure of nano-scale multilayers TiAlN/VN grown by unbalanced magnetron deposition. *J. Mater. Res.* **2004**, *19*, 1093–1104. [[CrossRef](#)]
29. Petrov, I.; Adibi, F.; Greene, J.E.; Hultman, L.; Sundgren, J.E. Average energy deposited per atom—A universal parameter for described ion-assisted film growth. *Appl. Phys. Lett.* **1993**, *63*, 36–38. [[CrossRef](#)]
30. Hoffman, R.W. Stress in thin films: The relevance of grain boundaries and impurities. *Thin Solid Films* **1976**, *34*, 185–190. [[CrossRef](#)]
31. Nix, W.D.; Clemens, B.M. Crystallite coalescence: A mechanism for intrinsic tensile stresses in thin films. *J. Mater. Res.* **1999**, *14*, 3467–3473. [[CrossRef](#)]
32. Freund, L.B.; Chason, E. Model for stress generated upon contact of neighbouring islands on the surface of a substrate. *J. Appl. Phys.* **2001**, *89*, 4866–4873. [[CrossRef](#)]
33. Janssen, G.C.A.M. Critical review: Stress and strain in polycrystalline thin films. *Thin Solid Films* **2007**, *515*, 6654–6664. [[CrossRef](#)]



© 2017 by the authors. Licensee MDPI, Basel, Switzerland. This article is an open access article distributed under the terms and conditions of the Creative Commons Attribution (CC BY) license (<http://creativecommons.org/licenses/by/4.0/>).